Probing precipitation in aluminium alloys during linear cooling via *in-situ* differential scanning calorimetry and electrical resistivity measurement

Zi Yang [a], Sina Mallow [b], John Banhart [a,*], Olaf Kessler [b,c]

[a] *Department of Microstructure and Residual Stress Analysis, Helmholtz-Zentrum Berlin, Hahn-Meitner-Platz 1, Berlin 10587, Germany*
[b] *Chair of Materials Science, Rostock University, Albert-Einstein-Str. 2, Rostock 18059, Germany*
[c] *Competence Centre °CALOR, Department Life, Light and Matter, Rostock University, Albert-Einstein-Str. 25, Rostock 18059, Germany*

A B S T R A C T

Investigating precipitation processes in aluminium alloys during cooling from the solutionising temperature is important because the level of solute supersaturation and the presence of pre-precipitated solutes determine the response to the subsequent age hardening step. Differential scanning calorimetry has been developed to a suitable method to follow precipitation over a wide range of cooling rates. We develop a device that allows us to measure electrical resistivity *in-situ* during the quenching of alloy samples from the solutionising temperature. A procedure is formulated that allows us to separate the signal related to precipitation from the large background caused by the temperature dependence of electrical resistivity. Application to an aluminium alloy 6014 reveals a two-stage precipitation reaction during cooling at rates between 1 and 20 K min^{-1}, the first related to precipitation of the stable β phase, the second due to the formation of various metastable phases. Comparison between resistivity and DSC signals measured at the same cooling rate shows very close correspondence between the two. Thus, in the future, both methods could be used in a complementary way.

1. Introduction

Precipitation is a fundamental phase transformation phenomenon in metallic materials and a commonly employed method for enhancing the strength, particularly of aluminium alloys. It occurs whenever a solutionised alloy is cooled to below the solubility limit of its alloying elements under non-equilibrium conditions and is further aged there. Driven by the reduction of the Gibbs free energy, solute atoms aggregate together after diffusing through the matrix and form secondary phases of various types, sizes, and number densities depending on the aging temperature and time, a process that has continuously been the subject of extensive research for a long time. Unless cooling is very fast, precipitation may start already in the cooling stage and continue during the actual age-hardening step after the end of quenching. Conventionally, both precipitation during cooling after a solution heat treatment and during subsequent ageing treatments are studied. The latter is normally conducted at lower temperatures and aims at achieving finely dispersed precipitates and maximising the hardening effect. In contrast, precipitation during quenching mainly takes place at higher temperatures and gives rise to coarser precipitate structures and lower hardening responses. Instead of contributing much to hardening directly, precipitation during quenching indirectly influences the hardening potential during ensuing ageing as it reduces solute supersaturation. Therefore, studies of precipitation during cooling contribute to the understanding of the quench sensitivity of alloys, which in turn provides a guidance for designing suitable quenching strategies [1].

To characterise the precipitation process during cooling various methods have been utilised. *Ex-situ* methods, in particular microscopy, provide valuable information on the nature of precipitation such as the type, morphology and formation mechanism of precipitates [2]. A recent study exploiting positron annihilation spectroscopy by some of the current authors was able to identify the microscopic state including vacancies by interrupting the quenching process at a given temperature [3]. One disadvantage of *ex-situ* characterisation is that it requires an interruption of cooling at a target temperature of interest and a freezing of the resulting structure. For each such target temperature, a new cooling experiment needs to be performed, which is an inconvenience in comparison with *in-situ* characterisations measuring the complete process in one run.

Common *in-situ* methods for characterising precipitation include small-angle scattering using X-rays or neutrons, differential scanning calorimetry (DSC), electrical resistivity measurement, dilatometry, X-

---

* Corresponding author.
E-mail address: banhart@helmholtz-berlin.de (J. Banhart).

ray diffraction and tomography [4]. Among those, DSC has been developed to a powerful method for cooling experiments [1,5,6]. Systematic studies on a variety of alloys, mostly Al-Mg-Si, have been carried out in a wide range of cooling rates (0.05 up to 20,000 K min^{-1}) in combination with other methods (various microscopy and hardness measurements) to clarify the precipitation sequence during cooling (often two precipitation regimes can be distinguished) and to determine the critical cooling rate above which no notable precipitation occurs anymore [6].

In contrast to DSC, measurement of electrical resistivity, although also a fast method, is rarely applied during cooling [7,8] although it has been frequently used in analysing isothermal ageing experiments [9,10]. One reason lies in the precise dynamic sample temperature control during cooling, which is readily accessible in DSC but not widely available for electrical resistivity samples, usually wires or thin strips. This matters because not only the process of precipitation depends on temperature, but also electrical resistivity is intrinsically temperature-dependent. To separate the contributions and focus on the precipitation-related electrical resistivity change, a custom-made cooling setup is required to measure and control the sample temperature *in-situ*. Archambault et al. [7] and Li et al. [8] have used setups to measure the electrical resistivity change in 7XXX alloys during linear and Newtonian (free, convective) cooling, respectively. However, the descriptions given of the important temperature control systems are rather brief, thus not allowing for reproduction and use of their devices for further applications.

We demonstrate the *in-situ* measurement of electrical resistivity during linear cooling with the help of heating plates, a set-up recently successfully used for linear heating experiments [11]. We describe both data acquisition and analysis in detail including the subtraction of the temperature-related resistivity of the matrix required to obtain the precipitation-related resistivity change. The results show very good agreement with *in-situ* DSC measurements during cooling.

2. Experimental

2.1. Electrical resistivity

2.1.1. Setup

A custom-made, electrically non-conducting ceramic heating plate (Fig. 1a) is used in this work for temperature regulation. A fan on the side ensures circulation of air and hence supports cooling of the device. Controlled cooling is realised by counter-heating through the heating plates against the air cooling. The heating power is regulated with the temperature feedback of an ungrounded thermocouple that passes through the lower heating plate and touches the sample. The resistance of the sample is recorded *in-situ* (i.e. at the respective temperature) using the four-point method, in which a constant current I of 0.1A is put through the sample and the corresponding voltage drop is measured, all

via a Keithley 2401 multimeter. Meanwhile, to cancel the offset voltage in the circuit, caused for instance by the thermoelectric effect, the polarity of the current is changed every ~0.8 s during the measurement. At each polarity, 10 voltages are sampled, and every four polarity reversals the average of all the measured voltages is calculated to yield the final value. Therefore, each resistance measurement takes ~3.5 s, which defines the acquisition rate during continuous cooling. These settings are not physically based but rather inherited from previous isothermal ageing measurements [12], thus leaving room for further improvements.

2.1.2. Samples

Commercial 6014 (0.65 wt.% Mg, 0.6 wt.% Si, 0.12 wt.% Cu, 0.18 wt.% Fe, 0.08 wt.% Mn) alloy was received from Novelis Inc. (Sierre, Switzerland) as a 1-mm thick sheet. This material has been already used in previous studies [3,11,13,14]. After rolling to 0.3 mm thickness, the samples are laser-cut into a meander shape (Fig. 1b). This shape helps to obtain a long conduction path on the limited area of the heating zone and therefore increases the sensitivity of the measurement. However, the undefined total length makes precise calculations of electrical resistivity (ρ) from the sample resistance (R) difficult. Therefore, the following method is applied for calculating the geometric factors of the meander-shaped specimens. First, we calculate the geometric factor of an annealed pure Al (5 N) meander sample by relating its resistance to the resistivity measured on a wire sample of a well-defined length made of the same material. The measurement on the wire is conducted using a conventional four-point probe setup immersed in an oil bath at 20 °C with 0.1 A current applied [15]. The diameter ($d_w = 0.84$mm) and length ($l_w = 454$mm) of the wire can be precisely measured, which allows for a calculation of its resistivity from its resistance R_w:

$$\rho_{Al, \ 20°C} = \frac{\pi d_w^{\ 2}}{4l_w} R_w. \tag{1}$$

This yields a resistivity of 2.66 μΩ•cm for pure Al wire which is in good accordance with the literature [16]. As the pure Al meander sample has the same resistivity, we can use it for calculating its geometric factor at 20 °C (g_0) from the resistance measured on the meander sample R_m at the same temperature:

$$g_0 = \frac{\rho_{Al, \ 20°C}}{R_m}. \tag{2}$$

At elevated temperatures, thermal expansion causes changes to the geometric factor, and to account for this, we apply a correction to the geometric factor using:

$$g_T = g_0 \cdot \varepsilon, \tag{3}$$

where ε is the ratio of the geometric factors at temperatures T and $T_0 = 20$ °C and can be calculated as $\varepsilon = 1 + \frac{\Delta L}{L_0}$, with $\frac{\Delta L}{L_0}$ the linear expansion ratio with respect to the length L_0 at 20 °C [17] .The discrete values of $\frac{\Delta L}{L_0}$ given by Simmons et al. [17] are interpolated for each temperature
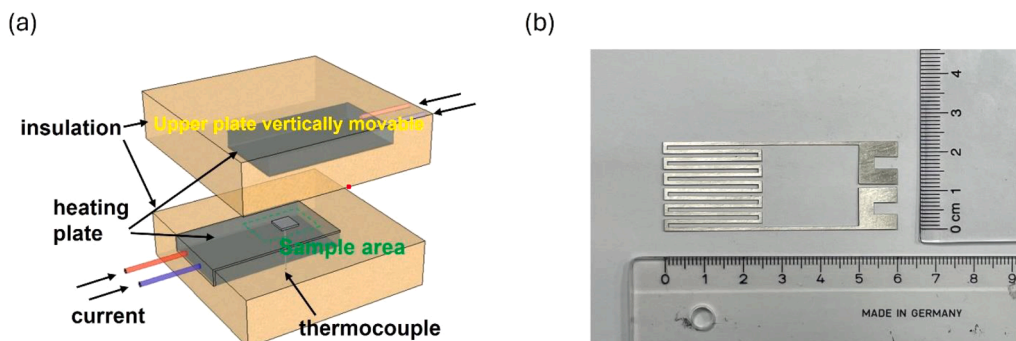

Fig. 1. (a) Schematic of the heating plate [11], and (b) the meander-shaped sample used in the study. The outer contacts are for the current, the inner ones for the voltage measurement.

measured in the study. Subsequently we can calculate the resistivity of the pure Al meander sample during cooling by

$$\rho_{Al} = g_T \cdot R_{Al}, \tag{4}$$

with R_{Al} the resistance measured on pure Al at any temperature during cooling.

Next, we calculate the geometric factor of the alloy meander specimen from the measured resistance R_{alloy}. However, it cannot be calculated in the same way as the pure Al meander sample since the alloy resistivity ρ_{alloy} is unknown due to the presence of Fraenkel's paper solutes and precipitates. However, by applying Matthiessen's rule we separate the dynamic contributions stemming from thermal vibrations, ρ_T, and the residual contributions coming from defects such as alloying elements (Mg, Si, Cu), dislocations, precipitates etc., ρ_d, and assume that the temperature dependent resistivity contribution is the same in pure Al and the alloy:

$$\rho_{Al} = \rho_T + \rho_{d,Al}, \tag{5}$$

$$\rho_{\text{alloy}} = \rho_T + \rho_{d,\text{alloy}}. \tag{6}$$

Therefore, with $\rho_{\text{alloy}} = g_{0,\text{alloy}} \cdot \varepsilon \cdot R_{\text{alloy}}$ we obtain the relationship between the measured resistance of the alloy and the resistivity of pure Al using:

$$\rho_{Al} = g_{0,\text{alloy}} \cdot \varepsilon \cdot R_{\text{alloy}} - \rho_{d,\text{alloy}} + \rho_{d,Al}. \tag{7}$$

In the above equation, temperature is an implicit variable, and the defect contributions ($\rho_{d,\text{alloy}}$, $\rho_{d,Al}$) are unknown and theoretically also dependent on temperature. However, when the changes of defect contributions are small compared to the temperature dependent term, e.g. towards the end of cooling when precipitation gets weak, we approximate the defect terms as constants, and the slope of ρ_{Al} plotted against $\varepsilon \cdot R_{\text{alloy}}$ at various temperatures gives the geometric factor of the alloy sample at 20 °C. This will be further illustrated in Section 3.

2.1.3. Cooling experiments

Each measurement contains a fast heating ramp up to 540 °C, an isothermal solutionising step for 20 min at 540 °C, and a cooling stage, during which the sample remains between the heating plates. The passive cooling curve with the heating plate turned off appears approximately exponentially decaying (Fig. 2a), just that the deviation of the derivative from the expected linear behaviour as a function of *T* expresses a non-exponential component (Fig. 2b). The derivative defines the upper limit of achievable cooling rates, which is a function of temperature. When turning on counter-heating, linear cooling at a given rate can be performed on the sample up to a critical temperature where the cooling rate limit is reached, and further cooling is non-linear. In this work, resistivity measurements are carried out at cooling rates from 1 K min^{-1} to 20 K min^{-1}. We use 5 meander-shaped samples, with multiple

measurements performed on each sample. For each cooling rate, at least 5 repeated measurements are carried out.

2.2. Differential scanning calorimetry

Two different calorimeters are used for cooling experiments: a Calvet-type heat-flux DSC (Setaram DSC 121, KEP TECHNOLOGIES SA, Mougins, France) for slow cooling rates (1 to 6 K min^{-1}) and a power-compensated DSC (PerkinElmer DSC 8500, Waltham, MA, USA) for the faster cooling rate of 20 K min^{-1}. Two different sample geometries are required (Fig. 3a,b). The base material is sheet metal of thickness 1.1 mm. For measurements in the heat-flux DSC, it is necessary to stack 9 discs (each Ø 6.0 mm) per sample to reach a sufficient sample mass (here 622 mg). A stacked sample could pose a challenge due to its notably higher surface-to-volume ratio, which may cause greater bending in the DSC curves as a result of heat radiation effects. Osten et al. have demonstrated quantitatively that DSC results from stacked discs are equal compared to compact cylinders in the case of heating aluminium alloys [18]. To ensure high comparability of the DSC results, the same DSC samples are used repeatedly for cooling rates 1 to 6 K min^{-1} and 20 K min^{-1} respectively. Since the sample mass required for the power-compensated DSC is much smaller, one disc from the stack is used (sample mass of 69 mg). All samples are enclosed in pure aluminium crucibles before inserting them into the calorimeters' micro-ovens. The samples are first heated to 540 °C at a heating rate of 18 K min^{-1} and then isothermally soaked there for 20 min. The reference sample chosen is made of pure aluminium (purity 99.9995 %) of dimensions comparable to the alloy samples. The adjustment of the reference masses is essential here. This can be done by measuring the absolute heat capacity of alloy 6014 and comparing it to that of the reference material. This results in a reference mass of 618 mg for the heat-flux DSC, and 68 mg for the power-compensated DSC.

To ensure high-quality raw data, it is crucial to eliminate the device-specific heat flow curvature. This can be achieved by measuring a so-called baseline. Pure aluminium references are placed into both micro-ovens for this purpose and subjected to the same temperature program used for the alloy samples. It is known that the device-specific curvature slightly changes with time, particularly in power-compensated DSC's. Therefore, the DSC measurements are carried out following the pattern "sample - baseline – sample". By subtracting the baseline data from the associated sample data, any device-specific curvature present can be effectively eliminated. Repeated cooling experiments are carried out in the following order: 6 K min^{-1} (2 measurements) à 1 K min^{-1} (2 measurements) à 6 K min^{-1} (2 measurements) à 3 K min^{-1} (1 measurement) à 20 K min^{-1} (4 measurements).

To compare measurements involving different cooling rates (β) and sample masses (m_S), normalisation of the measured heat flow to the excess specific heat capacity ($c_{p\text{excess}}$) is recommended. Therefore, $\dot{Q}_S$ and $\dot{Q}_{Bl}$ represent the sample and baseline heat flows: [19]
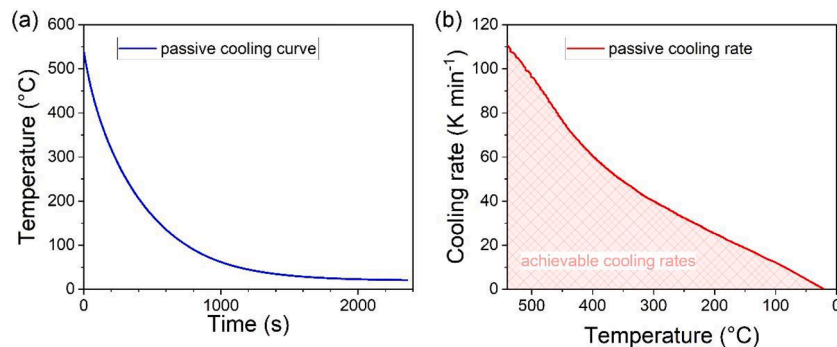

Fig. 2. (a) Passive cooling temperature profile plotted as a function of time, and (b) cooling rate plotted as a function of temperature as numerically derived from the former. The hatched area under the curve indicates cooling rates achievable by applying counter heating.
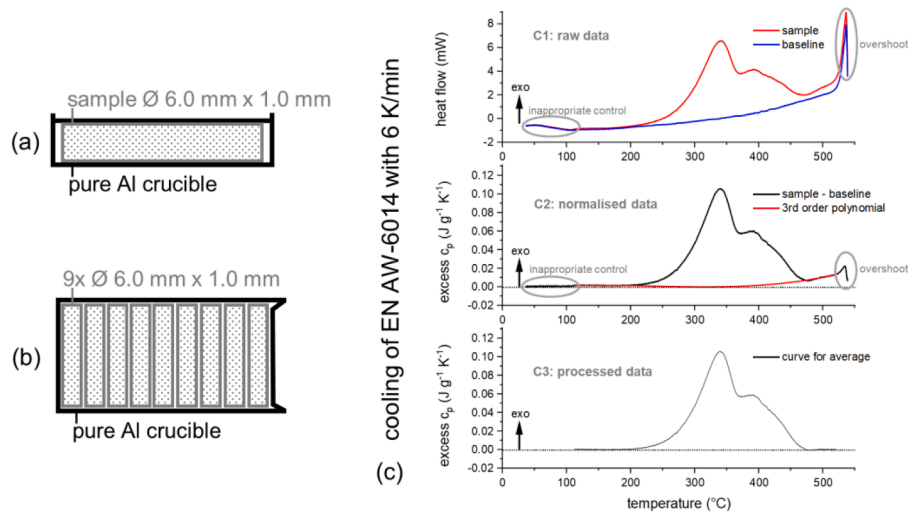
Fig. 3. Schematics for the single (a) and stacked (b) samples used for DSC measurements in different devices; (c) evaluation of the DSC data for the cooling experiment at 6 K min^{-1}.

$$c_{p_{excess}} = \frac{\dot{Q}_S - \dot{Q}_{Bl}}{m_S \cdot \beta}. \qquad (8)$$

Fig. 3c illustrates the data processing of the DSC curves based on a cooling curve with 6 K min^{-1}.

The first part shows the raw data (C1), which undergo an elimination of the device-specific curvature by subtracting the baseline from the sample measurement (C2). There is an overshoot at the beginning of the measurement, which is related to the change in control from isothermal to linear cooling. Furthermore, the end of the curve in the indicated area shows insufficient temperature control. These two parts of the curve should be discarded. The dotted lines indicate the related zero level. After cutting off the above artefacts, the beginning and end curve sections in Fig. 3c (C2) are assumed to be reaction-free zones. Therefore, the normalised curve is corrected by subtracting a third-order polynomial, which is fitted to the reaction-free zones. However, this approach is slightly subjective and requires cautious handling. One finally obtains the corrected data, Fig. 3c (C3). For each cooling rate, different curves

are now averaged. The evaluation is described in detail by Ref. [1]. Because of the high reproducibility of the DSC measurements and limited number of experiments, no standard deviations are shown. Due to the zero-level correction (subtraction of polynominal fitting), both data from DSC and resistivity measurement can be compared very well.

3. Processing of electrical resistivity data

An important part of the work lies in the processing of the raw data obtained from the measurements, i.e. temperature and resistance (voltage), and the extraction of the precipitation-related resistivity change as a function of temperature from the large background of temperature-dependent resistivity change. We explain in detail the complete procedure in this section. It includes the following steps: (1) synchronising the temperature and resistance data and obtaining the resistance change as a function of temperature during cooling; (2) calculating the geometric factor of the sample and converting the sample
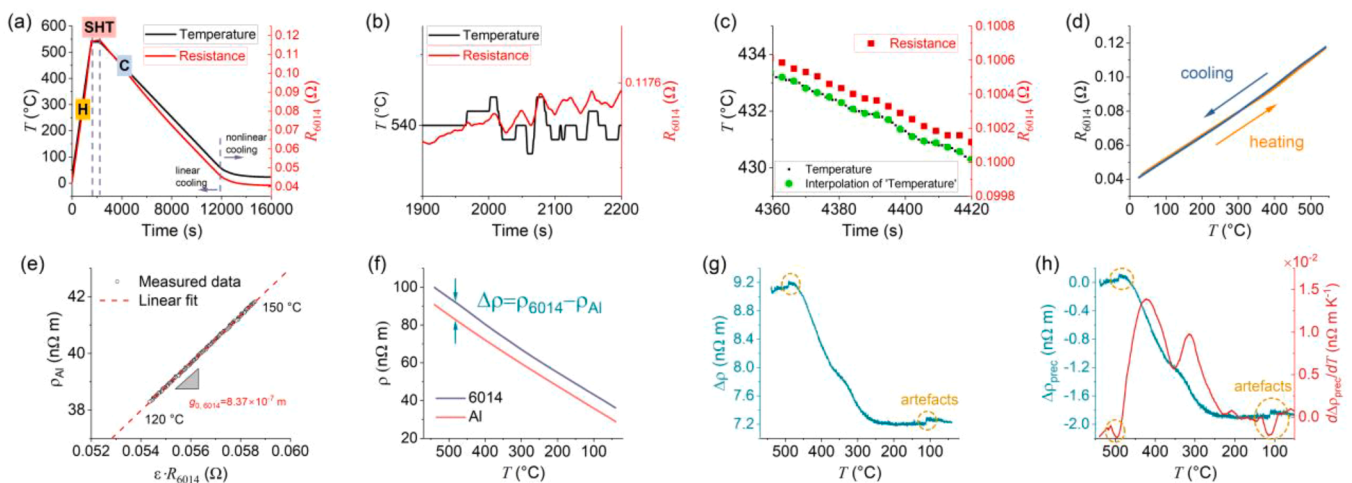

Fig. 4. Procedures of data processing. (a) Measured temperature T and resistance R_{6014} of the alloy sample as a function of time. (b) Enlarged view of solution annealing stage showing fluctuations of temperature and resistance. (c) Interpolation of temperature data according to the timestamps of resistance measurements. (d) Resistance evolution as a function of temperature for both the heating and cooling stages. (e) Resistivity of pure Al (ρ_{Al}) plotted as a function of the resistance of the 6014 sample (R_{6014}) measured during the same cooling below 200 °C to calculate the geometric factor of the 6014 alloy meander sample. (f) Resistivity evolution as a function of temperature for both 6014 alloy and pure Al at the same cooling rate. (g) Difference between the resistivity of the alloy sample and of pure Al, demonstrating the difference in the defect-related resistivity. (h) Precipitation-related resistivity change ($\Delta\rho_{prec}$) and its derivative with respect to temperature. Artefacts (in orange circles) sometimes occur due to contact issues between the thermocouple and the sample.

resistance to resistivity; (3) subtracting the temperature-related resistivity change.

Fig. 4 demonstrates the procedure using one example dataset. There, a sample is cooled at 6 K min^{-1} after heating to 540 °C at 20 K min^{-1} and solutionising for 10 min there (Fig. 4a). After synchronising the temperature and resistance data (Fig. 4b), we can plot the resistance vs. temperature. Here, due to a lower measurement frequency of resistance, we interpolate the temperature data at the timestamps of the resistance measurements (Fig. 4c). The resulting resistance vs. temperature during the whole thermal cycle is displayed in Fig. 4d. There, we already notice that the shapes of the resistance curves during heating and cooling are slightly different, reflecting the precipitation and dissolution reactions.

However, compared with the resistance change caused by the varying temperature, such deviation is too small to be observed clearly, which emphasizes the necessity to correct for the temperature-related resistivity change. This and the calculation of the geometric factor of the sample can be both done by relating to the resistivity change of a pure Al meander sample cooled applying the same profile, as mentioned in Section 2.1.2. This approach corresponds to the differential approach known from DSC. It assumes that the contributions of the temperature-dependent electrical resistivity (ρ_T) are the same in both pure Al and 6014 alloy samples. This assumption is especially true in the low-temperature regime, such as <200 °C, where precipitation during cooling of aluminium alloys is typically very weak [1]. In this temperature range, we plot the resistivity of pure Al versus the resistance of the alloy for the same temperatures. The slope informs us about the geometric factor of the meander-shaped alloy (Fig. 4e). The resistivities calculated after accounting for thermal expansion of both the alloy and the pure Al specimens are shown in Fig. 4f. The higher contribution from defects, such as solutes, dislocations, grain boundaries, precipitates etc. in the alloy sample are reflected in the overall higher resistivity. In the experiment under consideration (alloy 6014, cooling rate 6 K min^{-1}), this difference is reduced as the temperature is lowered (Fig. 4g) due to a decreasing amount of dissolved solute atoms, i.e. precipitation during cooling. After smoothing the curve and taking the derivative with respect to temperature, the 'rate' of such evolution is obtained (Fig. 4h) and can be later compared to the DSC trace. The quantity in this figure is called $\Delta\rho_{prec}$ because it is mainly caused by the precipitation of previously dissolved solutes as will be discussed in Section 4.2.

4. Results and discussion

4.1. DSC

The results of DSC are discussed first since they serve as reference measurements in this study and an interpretation of similar signals has already been given in the literature [2]. Fig. 5 presents the excess heat capacity of the alloy at various cooling rates. Two major exothermic peaks can be distinguished in the curves—a high-temperature reaction peak between 500 °C and 350 °C and a low-temperature one between 400 °C and 200 °C. The two peaks partially overlap, and their positions and magnitudes are influenced by the cooling rate. The high-temperature reaction has been attributed to the precipitation of the β-Mg$_2$Si phase, the low-temperature peak to precipitation of β'/B' particles [2]. The precipitation of the β phase is continuously suppressed as the cooling rate increases from 1 K min^{-1} to 20 K min^{-1}, as can be seen from the shift of the high-temperature peak to lower temperatures and the reduction of the peak magnitude. This is easily understandable since a shorter precipitation time is allowed when cooling faster. In contrast, the precipitation peak of β'/B' first shifts to higher temperatures and increases in intensity when the cooling rate increases from 1 K min^{-1} to 6 K min^{-1}. This behaviour is a result of the strong β precipitation at the slower cooling rate. This has consumed solutes, which are then no longer available for further precipitation. A further increase of the cooling rate decreases the amplitude of the β'/B' peak due to the suppression of the
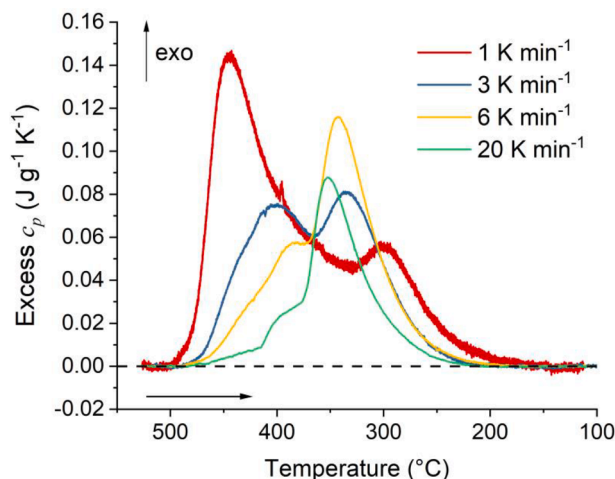

Fig. 5. DSC traces of the alloy 6014 at various cooling rates. Horizontal arrow indicates the direction of temperature progression, i.e. cooling.

overall precipitation kinetics. These results are in good accordance with the literature on other similar alloys [2].

4.2. Electrical resistivity

Fig. 6a displays the resistivity change at various cooling rates. Although the repeated measurements exhibit some deviations (larger as the cooling rate increases), a general behaviour can be observed. At each cooling rate, the resistivity change first decreases slowly as the temperature is reduced until a certain temperature is reached and the resistivity change starts to drop more rapidly. Except for cooling at 20 K min^{-1}, all the curves show at least two stages in this process. The resistivity change is nearly constant below 250 °C with values depending on the cooling rate (-3.2 nΩ m at 1 K min^{-1} versus -1.8 nΩ m at 20 K min^{-1}), pointing at a higher amount of solutes, i.e. an overall suppressed precipitation under the faster cooling.

The derivative of the resistivity change with respect to temperature informs us better about the two stages during cooling (Fig. 6b). Such curves show features very similar to the DSC traces (Fig. 5), namely the two partially overlapping peaks in different temperature regimes. In analogy to DSC, a higher cooling rate leads to a continuous shift to lower temperatures and reduction of the high-temperature peak. Moreover, the low-temperature peak is first enlarged and shifted to higher temperatures before its amplitude decreases again.

A direct comparison between the DSC and resistivity results is given in Fig. 7. Qualitatively a very good agreement is observed between the peaks in the DSC curves and resistivity change derivatives in terms of the shape and position of the peaks for all measured cooling rates. Such correspondence implies that their physical origins are the same, i.e. the high-temperature peak is due to the precipitation of β, and the low-temperature peak to precipitation of β'/B'. DSC measures the precipitation heat, whereas the residual electrical resistivity after subtraction of the thermal contribution represents a superposition of various contributions. Point defects such as vacancies (ρ_v) and substitutional atoms ρ_{sol}, line defects such as dislocations ρ_{dis}, grain boundaries (2D defects, ρ_{gb}) and volume defects such as small clusters ρ_{cl} and larger precipitates ρ_{ppt} might contribute to the total defect term:

$$\rho_d = \rho_v + \rho_{sol} + \rho_{dis} + \rho_{gb} + \rho_{cl} + \rho_{ppt} + \cdots \tag{9}$$

Vacancies contribute to residual resistivity with 19 nΩm at.%$^{-1}$ [20] compared to solute atoms such as Mg where the contribution is 4.44 nΩm at.%$^{-1}$. However, the vacancy site fraction even directly after solutionising and water quenching will be just around 7.5×10^{-5} [21]. After slower quenching (rate of 300 K min^{-1}, i.e. still 15 times faster than
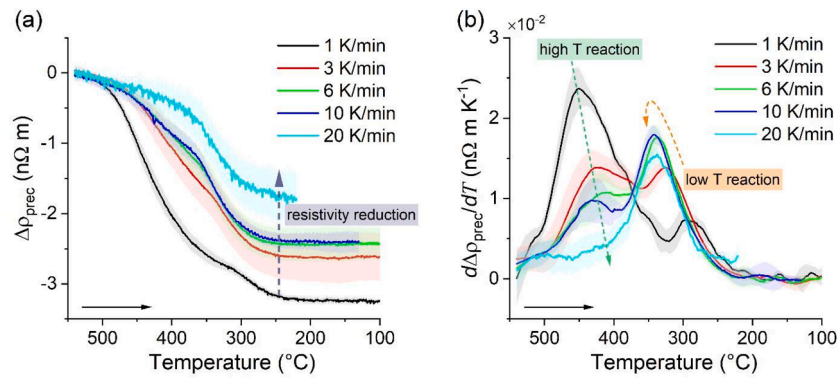
Fig. 6. (a) Evolution of precipitation-related resistivity change during linear cooling of alloy 6014 at various rates. (b) Rate of the resistivity change. (a,b) Averages (lines) and standard deviations of at least five experiments (highlighted bands) are given. Dashed arrows show trends of the characteristics with an increasing cooling rate. Horizontal arrows indicate the direction of the process.
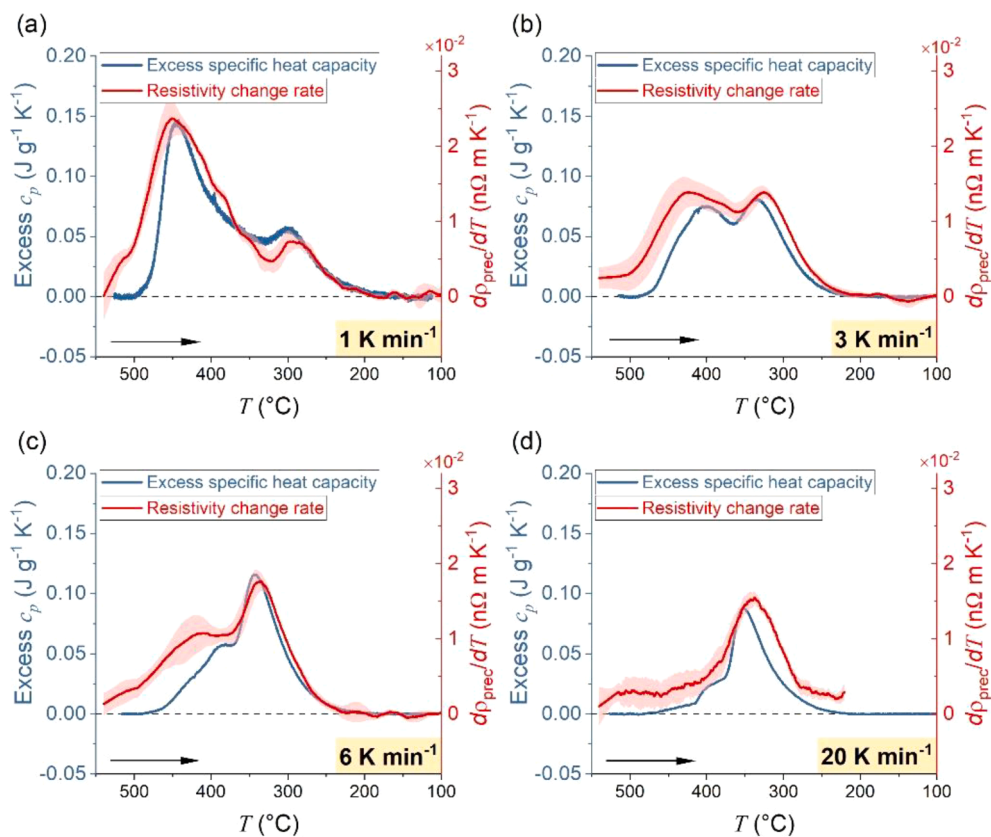

Fig. 7. Comparison of DSC and resistivity change rate for each cooling rate. (a) 1 K min⁻¹, (b) 3 K min⁻¹, (c) 6 K min⁻¹, (d) 20 K min⁻¹. Arrows in the plots indicate the direction of the process.

the rates applied in this work) the vacancy site fraction is below 2×10^{-6} [3]. In contrast, the fraction of Mg atoms is 6×10^{-3}, which implies that the contribution to resistivity from solutes is 3 orders (or more) of magnitude larger than that of vacancies, $\rho_v \ll \rho_{sol}$.

Dislocations and grain boundaries, ρ_{dis}, ρ_{gb}, can be shown to contribute little given their low numbers after solutionising at 540 °C and their small resistivity coefficients [22]. In contrast, atomic clusters can have a very pronounced "anomalous" effect on electrical resistivity, ρ_{cl}, as long as they are small (typical radius 1 nm) and occur in a high number densitiy such as during natural ageing of Al-Mg-Si alloys. Large total resistivity increases by up to 15 % have been observed during natural ageing (at 77 K) [23]. However, for ageing temperature around 120 °C or higher, a resistivity increase is no longer observed and an

immediate resistivity decrease [6] or a strong decrease after a just very short and small increase [24,25] occurs after the onset of ageing. The reason is that aging at higher temperatures leads to larger and less frequent precipitates [24]. In the current study, we cool rather slowly from the solutionising temperature and spend time at higher temperatures where instead of the formation of nm-sized clusters as during natural ageing larger precipitates are formed [24] that do not lead to a large anomalous resistivity increase.

The fact that isothermal ageing at high temperatures almost immediately decreases resistivity shows that the change caused by the removal of solutes from the matrix $\Delta\rho_{sol}$ (resistivity decrease) and their introduction into precipitates $\Delta\rho_{ppt}$ (potential resistivity increase) is dominated by the effect of solutes. The contributions of the precipitates

ρ_{ppt} depend on their sizes and number densities. Raeisinia et al. [26,27] estimated contributions from various precipitates formed during isothermal ageing from 180 °C to 480 °C and found that the contribution to resistivity becomes very small when ageing at higher temperatures due to large precipitate sizes, i.e. $\rho_{ppt} \ll \rho_{sol}$.

Quantitatively, some differences between the measured DSC and resistivity signals can still be discerned. The exact temperatures of the precipitation peaks in the resistivity change rate curves appear slightly different from those in the corresponding DSC curves. In addition, the width of the peaks, in particular the high-temperature peak, is larger in the resistivity measurement. Some of these observed differences might be due to the neglected influence of early precipitation on the electrical resistivity or to thermal heterogeneities or thermal offsets in the experiment, which could be removed in future set-ups.

If we plot the precipitation-related resistivity decrease as a function of the integrated heat of the DSC trace Δq_{prec}, defined as

$$\Delta q_{\text{prec}} = \int_{T}^{T_0} c_{p_{\text{excess}}} \, dT, \tag{10}$$

we find that the data for all measured cooling rates show similar trends and fall nearly onto the same master curve (Fig. 8), again pointing at a common physical background. The master curve features first a resistivity reduction with a less pronounced heat effect in the very early stage and subsequently an approximately linear correlation. This early drop in the curve reflects the discrepancy found between the two rate curves in the high-temperature regime in Fig. 7. Its physical origin is still unclear. One reason may be the different sensitivities of the two experimental setups for early precipitation reactions.

The approximate linearity of the relationship deserves some discussion. It implies that the resistivity change and the heat effect strongly depend on each other. A drop of 1 nΩm in ρ_{prec} corresponds to a heat generation of approximately 6 J g^{-1}. The precipitation heat of a given type of precipitate is often considered proportional to its volume fraction. First-principles calculations give a molar formation enthalpy of 32.4 kJ per mole of solute in the β' (Mg$_9$Si$_5$) phase and 36.4 kJ per mole of solute in the β (Mg$_2$Si) phase (difference between pure solid solution and solid solution with embedded precipitate) [28]. Another work gives a similar but slightly higher value for the β phase [31].

As discussed above, the resistivity change caused by the re-grouping of solutes during precipitation $\Delta\rho_{prec}$ is dominated by the effect of solute depletion of the matrix:
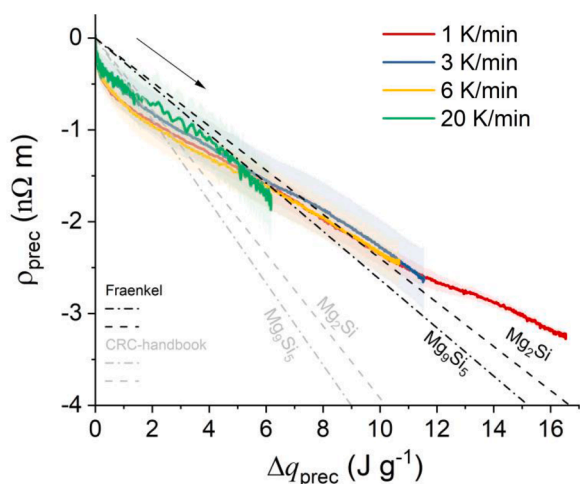
$$\Delta\rho_{\text{prec}} = \Delta\rho_{\text{ppt}} + \Delta\rho_{\text{sol}} \approx \Delta\rho_{\text{sol}}. \tag{11}$$

For the solute contribution to resistivity, a linear and additive relationship to the solute content can be assumed whenever the concentrations are small:

$$\rho_{sol} = \sum_i c_i \rho_i, \tag{12}$$

where c_i are the concentrations of solute type i, and ρ_i are the contributions to resistivity per unit concentration [32]. Therefore, one can construct the relationship between $\Delta\rho_{sol}$ and Δq_{prec},

$$\frac{\Delta\rho_{\text{sol}}}{\Delta q_{\text{prec}}}_{[Mg_xSi_y]} = -\varphi \cdot (x+y)^{-1} \cdot \Delta H_{[Mg_xSi_y]}^{-1} \cdot (x\rho_{\text{Mg}} + y\rho_{\text{Si}}), \tag{13}$$

where φ is the molar weight of the alloy ($\approx$27 g mol^{-1}), and $\Delta H_{[Mg_xSi_y]}$ the molar formation enthalpies of the phase Mg$_x$Si$_y$ (per mole of solutes). Δq_{prec} is the integrated DSC signal.

Various characteristic ρ_i values for Mg and especially Si have been measured or calculated [32–34]. Taking values listed by Mondolfo [35] who refers to Fraenkel [30] (ρ_{Mg} = 4.44 nΩm at.%$^{-1}$ and ρ_{Si} = 0.83 nΩm at.%$^{-1}$ after translation from wt.% to at.%) and the molar formation enthalpies of the phases mentioned above, we find the calculated linear relationships for both β'-Mg$_9$Si$_5$ and β-Mg$_2$Si phases similar and close to the experimental curves. However, there seems to be an inconsistency between the specific solute resistivity contribution as given by Mondolfo and by Fraenkel and the value also appears very low compared to other sources as documented in the CRC handbook [29] or in Ref. [32]. In particular, its value for Si is at the lower end of the range reported in Ref. [32] (0.8 to 20 nΩm wt.%$^{-1}$). After taking an intermediate value set (ρ_{Mg} = 4.4 nΩm at.%$^{-1}$ and ρ_{Si} = 6.95 nΩm at.%$^{-1}$), much higher slopes are obtained for the calculated linearities than for the experimental results. The contributions of the precipitates that are in the first place ignored could partially compensate for the observed discrepancies although their fractions are expected to be rather small. Other factors influencing the calculations include the temperature dependence of the specific resistivity contribution of the solutes i.e. a deviation from Matthiessen's rule [21]. This remains to be explored.

4.3. Outlook on further improvements

The instrumental setup originally built for performing heating experiments can be turned into measuring the electrical resistivity *in-situ* during linear cooling. The precipitation process evaluated by resistivity measurement qualitatively agrees with the DSC signal when cooling aluminium alloy 6014 from the solution annealing temperature at rates ranging from 1 to 20 K min^{-1}. Further improvements of the setup are possible.

First, the sampling frequencies of the temperature and resistance measurements could be enhanced in future experiments, especially when higher cooling rates beyond the ones currently used are required. This could yield a smoother curve and reduce the bias caused by the progression of reaction between polarity reversals [36].

The second potential improvement lies in the maximum achievable cooling rate, which depends on the cooling capacity of the setup (Fig. 2). In the current work and alloy, precipitation down to 200 °C is of interest. This corresponds to a maximum cooling rate of ~20 K min^{-1} with the air circulation used. Higher cooling rates can still be achieved at higher temperatures but such experiments might not cover the whole precipitation process during cooling. To overcome this limitation requires modifications to the setup. Possible solutions include using pre-cooled gas to enlarge the temperature gradient or lowering the total heat capacity of the system, for example by miniaturising the device.

Another advantage of miniaturising the sample is related to the thermal homogeneity across the sample. In previous work on the setup,

Fig. 8. Precipitation-related resistivity reduction versus DSC heat integral for alloy 6014. Dashed lines represent the $\Delta\rho_{sol}$ vs. Δq_{prec} relationships for two typical phases using values given in Refs. [28–30].

Erdle et al. [37]. identified a gradient of ~3 K across the centre area of the heating plate. This appears to be in agreement with the difference between the resistivities measured on pure Al in our study and the reference values measured by Simmons et al. [38] (Fig. 9). The deviations from the reference values are all smaller than 0.4 nΩ m. Considering a temperature coefficient of ~0.11 to 0.13 nΩ•mK^{-1}, this indicates that the overall temperature of the sample is ~3 K higher than at the location of the thermocouple. However, it is still possible that in some areas of the sample the temperature exceeds this value as the resistivity measured is an averaged property of the whole sample. Since precipitation is temperature dependent, the consequence of thermal inhomogeneity is a smoother curve in Fig. 6a or broader peaks in Fig. 6b than they are supposed to be. Miniaturising the sample could lead to a more uniform temperature.

Finally, measurement artefacts (Fig. 4h) caused by thermal contact issues can be solved by welding the thermocouple to the meander sample. Avoiding any alloying effect caused by welding requires only a small modification of the meander layout, with an extra lead that conducts heat but is not in the path of the electric current.

Such an improved setup for the *in-situ* measurement of electrical resistivity may pave the way to extending continuous-cooling precipitation (CCP) diagrams of aluminium alloys to higher cooling rates. Up to now, directly measured CCP diagrams are limited to typical a few K s^{-1}, which is the upper cooling rate limit of conventional DSC [1]. Cooling rates above ~1000 K s^{-1} are accessible by Differential Fast Scanning Calorimetry (DFSC) on microchip-based sensors with μm-sized samples [39]. However, the cooling rate range between ~1 K s^{-1} and ~1000 K s^{-1}, which is relevant in quenching processes especially of high-alloyed 2XXX and 7XXX materials, is not accessible by direct cooling measurements. Currently, only indirect measurements like rapid cooling in a quenching dilatometer and interpreting the DSC reheating curves can give some insight [40].

5. Conclusions

A device has been designed and tested that allows us to measure *in-situ* during cooling from the solutionising temperature the part of electrical resistivity of an alloy that is related to precipitation. A first application to the aluminium alloy 6014 (Al-Mg-Si) shows:

The resistivity signal exhibits two features, each one representing one of the two known precipitation steps, first of stable β phase, then of metastable β' or B' phase particles. Depending on the cooling rate, the first or the second reaction dominates as it is also known from DSC studies.

Although DSC measures the heat generated by phase formation and electrical resistivity measures mainly the depletion of solutes from the solid solution, the two signals are *qualitatively* very similar. The reason is that solute depletion of the matrix and precipitation are connected physical processes. Electrical resistivity and DSC traces reproduce the temperatures and relative contributions of the two reactions in good *quantitative* agreement.

CRediT authorship contribution statement

Zi Yang: Writing – original draft, Validation, Methodology, Investigation, Formal analysis, Data curation, Conceptualization. **Sina Mallow:** Validation, Methodology, Investigation, Formal analysis, Data curation. **John Banhart:** Writing – review & editing, Validation, Supervision, Resources, Conceptualization. **Olaf Kessler:** Writing – review & editing, Validation, Supervision, Resources, Conceptualization.

Declaration of competing interest

The authors declare that they have no known competing financial interests or personal relationships that could have appeared to influence the work reported in this paper.
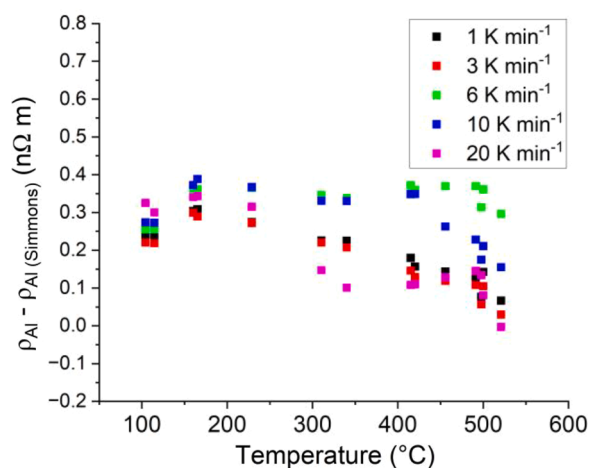

Fig. 9. Resistivities of pure Al measured in this study compared with the values in Ref. [38].

Data availability

The raw and the processed resistivity data required to reproduce these findings are available to download from Mendeley data [41].

References

[1] B. Milkereit, M.J. Starink, P.A. Rometsch, C. Schick, O. Kessler, Review of the quench sensitivity of aluminium alloys: analysis of the kinetics and nature of quench-induced precipitation, Materials 12 (2019) 4083.

[2] B. Milkereit, N. Wanderka, C. Schick, O. Kessler, Continuous cooling precipitation diagrams of Al-Mg-Si alloys, Mater. Sci. Eng. A 550 (2012) 87–96.

[3] Z. Yang, X.H. Jiang, X.P. Zhang, M. Liu, Z.Q. Liang, D. Leyvraz, J. Banhart, Natural ageing clustering under different quenching conditions in an Al-Mg-Si alloy, Scr. Mater. 190 (2021) 179–182.

[4] A. Deschamps, C. Hutchinson, Precipitation kinetics in metallic alloys: experiments and modeling, Acta Mater. 220 (2021) 117338.

[5] B. Milkereit, O. Kessler, C. Schick, Recording of continuous cooling precipitation diagrams of aluminium alloys, Thermochim. Acta 492 (2009) 73–78.

[6] B. Milkereit, M.J. Starink, Quench sensitivity of Al-Mg-Si alloys: a model for linear cooling and strengthening, Mater. Des. 76 (2015) 117–129.

[7] P. Archambault, D. Godard, High temperature precipitation kinetics and TTT curve of a 7xxx alloy by in-site electrical resistivity measurements and differential calorimetry, Scr. Mater. 42 (2000) 675–680.

[8] H.Y. Li, J.J. Liu, W.C. Yu, D.W. Li, Development of non-linear continuous cooling precipitation diagram for Al-Zn-Mg-Cu alloy, Mater. Sci. Technol. 31 (2015) 1443–1451.

[9] C. Panseri, T. Federighi, A resistometric study of preprecipitation in an aluminium-1.4% Mg$_2$Si alloy, J. Inst. Met. Lond. 94 (1966) 99–197.

[10] C. Panseri, T. Federighi, A resistometric study of pre-precipitation in Al-10-Percent Zn, Acta Metall. 8 (1960) 217–238.

[11] Z. Yang, I. Erdle, C.H. Liu, J. Banhart, Clustering and precipitation during linear heating in Al-Mg-Si alloys, J. Mater. Sci. Technol. 120 (2022) 78–88.

[12] J. Kühn, Investigation of clustering in Al-Mg-Si alloys by resistivity measurement. Master Thesis, Technical University Berlin, 2013.

[13] Z. Yang, Z.Q. Liang, D. Leyvraz, J. Banhart, Effect of pre-ageing on natural secondary ageing and paint bake hardening in Al-Mg-Si alloys, Materialia 7 (2019) 100413 (Oxf).

[14] Z. Yang, X.C. Zheng, Z.Q. Liang, J. Banhart, Refreshing industrially processed 6xxx series aluminum alloys after prolonged natural aging, Adv. Eng. Mater. 25 (2023) 2301102.

[15] Z. Yang, Multi-stage ageing in an Al-Mg-Si alloy, PhD Thesis, Technische Universität Berlin, Berlin, 2019.

[16] C.S. Taylor, L.A. Willey, D.W. Smith, J.D. Edwards, The properties of high purity aluminum, Met. Alloy. 9 (1938) 189–192.

[17] R.O. Simmons, R.W. Balluffi, Measurements of equilibrium vacancy concentrations in aluminum, Phys. Rev. 117 (1960) 52–61.

[18] J. Osten, B. Milkereit, C. Schick, O. Kessler, Dissolution and precipitation behaviour during continuous heating of Al-Mg-Si alloys in a wide range of heating rates, Materials 8 (2015) 2830–2848.

[19] S.M. Sarge, G.W.H. Höhne, W.F. Hemminger, Fundamentals Instrumentation and Applications, Wiley-VCH Verlag GmbH & Co. KGaA, Weinheim, Germany, 2014.

[20] M. Celasco, F. Fiorillo, P. Mazzetti, Thermal-equilibrium properties of vacancies in metals through current-noise measurements, Phys. Rev. Lett. 36 (1976) 38–42.

[21] M. Madanat, M. Liu, X.P. Zhang, Q.N. Guo, J. Cizek, J. Banhart, Co-evolution of vacancies and solute clusters during artificial ageing of Al-Mg-Si alloys, Phys. Rev. Mater. 4 (2020) 063608.

[22] F.R. Fickett, Aluminum .1. Review of resistive mechanisms in aluminum, Cryogenics 11 (1971) 349–367.

[23] S. Ceresara, E. Di Russo, P. Fiorini, A. Giarda, Effect of Si Excess on Ageing Behaviour of Al-Mg$_2$Si0.8% Alloy, Mater. Sci. Eng. 5 (1969) 220–227. -70.

[24] S. Esmaeili, D. Vaumousse, M.W. Zandbergen, W.J. Poole, A. Cerezo, D.J. Lloyd, A study on the early-stage decomposition in the Al-Mg-Si-Cu alloy AA6111 by electrical resistivity and three-dimensional atom probe, Philos. Mag. 87 (2007) 3797–3816.

[25] I. Kovács, J. Lendvai, E. Nagy, The mechanism of clustering in supersaturated solid solutions of Al-Mg$_2$Si Alloys, Acta Metall. 20 (1972) 975–983.

[26] B. Raeisinia, A study of precipitation in the aluminum alloy AA6111. Department of Metals and Materials Engineering, The University of British Columbia, 2003. Master thesis.

[27] B. Raeisinia, W.J. Poole, D.J. Lloyd, Examination of precipitation in the aluminum alloy AA6111 using electrical resistivity measurements, Mater. Sci. Eng. A 420 (2006) 245–249.

[28] M.A. van Huis, J.H. Chen, H.W. Zandbergen, M.H.F. Sluiter, Phase stability and structural relations of nanometer-sized, matrix-embedded precipitate phases in Al-Mg-Si alloys in the late stages of evolution, Acta Mater. 54 (2006) 2945–2955.

[29] K. Schröder, CRC Handbook of Electrical Resistivities of Binary Metallic Alloys, CRC, Boca Raton, FL, 1983.

[30] W. Fraenkel, W. Bosshard, On the conductivity of aluminium solid solutions, J. Inst. Met. 53 (1933) 694.

[31] C. Ravi, C. Wolverton, First-principles study of crystal structure and stability of Al-Mg-Si-(Cu) precipitates, Acta Mater. 52 (2004) 4213–4227.

[32] P. Olafsson, R. Sandstrom, A. Karlsson, Comparison of experimental, calculated and observed values for electrical and thermal conductivity of aluminium alloys, J. Mater. Sci. 32 (1997) 4383–4390.

[33] Y. Fukai, Electrical resistivity due to vacancies and impurities in aluminum: band structure effects in the defect scattering in polyvalent metals, Phys. Lett. 27A (1968) 416–417.

[34] S. Komatsu, S. Fujikawa, Electrical resistivity of light metals and alloys-Its measurement, interpretation and application. Part2: interpretation for measured values in commercial alloys and some applications, J. Jpn. Inst. Light Met. 47 (1997) 396–406.

[35] L.F. Mondolfo. Aluminum Alloys: Structure and Properties, Butterworths, Boston, 1976, p. 97.

[36] V. Garcia-Vazquez, Biased four-point probe resistance, Rev. Sci. Instrum. 88 (2017) 114701.

[37] I. Erdle, Nicht-isotherme Aushärtung einer 6014 Aluminiumlegierung. Master Thesis, Technical University Berlin, 2019.

[38] R.O. Simmons, R.W. Balluffi, Measurements of the high-temperature electrical resistance of aluminum: resistivity of lattice vacancies, Phys. Rev. 117 (1960) 62–68.

[39] B. Yang, B. Milkereit, Y. Zhang, P.A. Rometsch, O. Kessler, C. Schick, Continuous cooling precipitation diagram of aluminium alloy AA7150 based on a new fast scanning calorimetry and interrupted quenching method, Mater. Charact. 120 (2016) 30–37.

[40] H. Fröck, M. Reich, B. Milkereit, O. Kessler, Scanning rate extension of conventional DSCs through indirect measurements, Materials 12 (2019) 1085.

[41] Z. Yang, S. Mallow, J. Banhart, O. Kessler, Data of *in-situ* electrical resistivity measurements during linear cooling of Al alloys, Mendeley Data, (2024), V1. doi:10.17632/t8jsndsmwd.1.